Shape-based Feature Engineering for Solar Flare Prediction

Varad Deshmukh[1], **Thomas Berger**[2], **James Meiss**[3], **and Elizabeth Bradley**[1,4]

[1]Department of Computer Science, University of Colorado Boulder, Boulder CO 80309
[2]Space Weather Technology Research and Education Center, Boulder CO 80309
[3]Department of Applied Mathematics, University of Colorado Boulder, Boulder CO 80309
[4]The Santa Fe Institute, Santa Fe NM 87501
{varad.deshmukh, thomas.berger, james.meiss, elizabeth.bradley}@colorado.edu

Abstract

Solar flares are caused by magnetic eruptions in *active regions* (ARs) on the surface of the sun. These events can have significant impacts on human activity, many of which can be mitigated with enough advance warning from good forecasts. To date, machine learning-based flare-prediction methods have employed physics-based attributes of the AR images as features; more recently, there has been some work that uses features deduced automatically by deep learning methods (such as convolutional neural networks). We describe a suite of novel shape-based features extracted from magnetogram images of the Sun using the tools of computational topology and computational geometry. We evaluate these features in the context of a multi-layer perceptron (MLP) neural network and compare their performance against the traditional physics-based attributes. We show that these abstract shape-based features outperform the features chosen by the human experts, and that a combination of the two feature sets improves the forecasting capability even further.

Introduction

Solar flares are caused by rearrangement of magnetic field lines in active regions (ARs) on the surface of the Sun. These bright flashes arise from the collision of accelerated charged particles with the lower solar atmosphere. The coronal mass ejections (CMEs) that can accompany these events can have a significant impact on a range of human activity: damaging spacecraft, creating radiation hazards for astronauts, interfering with GPS, and causing power grid failures, among other things. Lloyd's has estimated that a power outage from an event associated with a powerful solar flare could produce an economic cost of 0.6 to 2.6 trillion dollars (Maynard, Smith, and Gonzalez 2013). Many of these losses could be mitigated with enough advance accurate warning of impending solar flares and the accompanying CMEs through actions such as switching to higher frequency radio for over-the-horizon communications with international airline flights, preparing satellites in orbit for safe-mode operations, and bringing additional generation capacity online to balance power grids against possible geomagnetically induced current disturbances. Since we currently lack these accurate advanced warnings, research into how to create them is a high priority.

Strategies for flare forecasting rest on the fact that the complexity of the magnetic field in an AR is known to be relevant to solar-flare occurrence. Figure 1 shows three observations at different times of the line-of-sight (LOS) magnetic field—called a *magnetogram*—observed from the sunspot AR 12673 as it evolved from a simple configuration as seen in panel (a) to more complex configurations seen in panels (b) and (c). The white and dark regions represent the LOS magnetic field exiting and entering the Sun's surface (termed positive and negative polarity, respectively). This particular AR produced a powerful flare within 24 hours of the complex mixed-polarity state observed in panel (b).

It is no surprise that these kinds of magnetic field observations have played a central role in machine learning-based forecasting models for solar flares. Typically, this has involved the use of features that solar-physics experts consider to be revelant to solar flaring, such as the magnetic field or electric current strength, current helicity, magnetic shear, and the like.[1] Recently, there has been a push to use convolutional neural networks (CNNs) to automatically learn latent features that are statistically correlated to the occurence of a solar flare. In this work, we take a wholly different approach, defining a novel feature set based purely on the shapes of the structures in the magnetogram. We formally quantify the complexity of an active region by using *computational geometry* and *computational topology* techniques on the radial component of the photospheric magnetic field, focusing specifically on the proximity and interaction of the polarities, as well as the components and holes in sub-level thresholded versions of the magnetogram image. Following a brief review of ML-based flare forecasting work and a description of the data, we present the results of a comparative study about the efficacy of these features in a multi-layer perceptron model.

In operational space weather forecasting offices, human forecasters currently use the McIntosh (McIntosh 1990) or Hale (Hale et al. 1919) classification systems to categorize active regions into various classes; they then determine the statistical 24-hour flaring probability derived from histor-

---

[1]Please refer to Table 1 of Deshmukh et al. (2020) for a complete list and to Bobra et al. (2014) for details about the associated calculations.
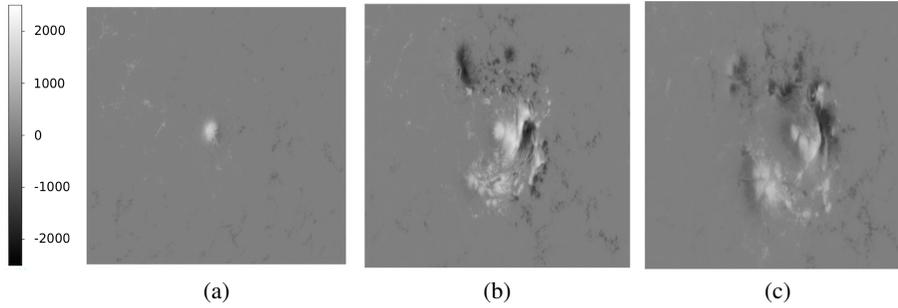
Figure 1: Three observations of line-of-sight magnetograms of sunspot #AR 12673, which produced multiple major (M-class and X-class) flares as it crossed the disk of the Sun in September 2017: (a) at 0000 UT on 9/1, (b) at 0900 UT on 9/5, about 24 hours before producing an X-class solar flare, and (c) at 1000 UT on 9/7, around the time of an M-class flare.

ical records (Crown 2012). Over the past decade, significant effort has been devoted to machine-learning solutions to this problem, including support vector machines (SVM) (Bobra and Couvidat 2015; Boucheron, Al-Ghraibah, and McAteer 2015; Nishizuka et al. 2017; Yang et al. 2013; Yuan et al. 2010), multi-layer perceptron (MLP) models (Nishizuka et al. 2018), Bayesian networks (Yu et al. 2010), logistic regression (Yuan et al. 2010), LASSO regression (Campi et al. 2019), linear classifiers (Jonas et al. 2018), fuzzy C-means (Benvenuto et al. 2018) and random forests (Campi et al. 2019; Nishizuka et al. 2017). Recently, the ML-based flare forecasting community has turned to deep learning methods for automatically extracting important features from raw image data that are relevant for flare-based classification (Chen et al. 2019; Huang et al. 2018; Park et al. 2018; Zheng, Li, and Wang 2019). The work cited in this paragraph is only a representative subset of ongoing research in this active field; for a more complete bibliography, please refer to Deshmukh et al. (2020).

In this paper, we use magnetograms from the Helioseismic and Magnetic Imager (HMI) instrument onboard NASA's Solar Dynamics Observatory (SDO), which has been deployed since 2010. Rectangular cutouts of each AR on the disk of the sun in each of these images, termed Spaceweather HMI Active Region Patches (SHARPs)—three examples of which make up Figure 1—are available to download from the Joint Space Operations Center website (jsoc.stanford.edu/). The metadata that accompanies each SHARP record contains values for the physics-based features mentioned above: i.e., the attributes that domain experts consider meaningful for the physics of the system. The dataset for the study reported in this paper, which covers the period from 2010-2016 at a one-hour cadence, focuses specifically on the radial magnetic field component from these images because of its role in magnetic reconnection.

The active regions in this dataset—which contains about 2.6 million data records, each approximately 2 MB in size, totaling 5 TB of data—are known to have produced about 1250 major flares within 24 hours of the image time (Schrijver 2016). We use the NOAA Geostationary Operational Environment Satellite (GOES) X-ray Spectrometer (XRS) flare catalog to identify these events and label the associated SHARP with a 1 if it produced a major flare—one whose peak flux in the 1-8 Å range is greater than $10^{-5}W/m^2$—in the 24 hours following the time of the sample, and 0 otherwise. Next, we discard all the magnetogram images that contain invalid pixel data (NaN values). The resulting data set included 3691 active regions, of which 141 produced at least one major flare as they crossed the Sun's disk and 3550 did not. This corresponded to $438,539$ total magnetograms, of which 5538 and 432821, respectively, were labeled as flaring and non-flaring.

A large positive/negative imbalance like this (78:1) is an obvious challenge in a binary classification machine-learning problem, as described at more length below. Another issue is that multiple images are available from a single AR during the run-up to a particular flare. To avoid artificially boosting our model accuracy by, for example, testing on an image that is one hour earlier than, and thus very similar to, an image in the training set, we perform an additional check each time we split the data into training (70%) and testing (30%) sets to ensure that all the magnetogram images belonging to a given AR are grouped together and placed either in the training or the testing set. 10 different random seeds are used for shuffling the data to generate 10 training/testing set combinations.

Shape-based Featurization of Active Regions

As in many machine-learning problems, the choice of features is critical here. Quantitative comparison studies show that none of the methods described above that use physics-based features extracted from magnetic field data are significantly more skilled—and indeed are typically less skilled—than current human-in-the-loop operational forecasts (Barnes et al. 2016; Leka et al. 2019a,b). In other words, while the physics-based attributes are no doubt important, they may not necessarily form an effective feature set for solar-flare forecasting.

The novelty of our work is our approach to the feature-engineering task from a mathematical standpoint, rather than a physics-based one. Specifically, we use computational

topology and computational geometry to extract features that are based purely on the shapes of the regions in the magnetograms. The underlying conjecture is that this is a useful way to capture the complexity of these regions—which is known to be related to flaring. As preliminary evidence in favor of that conjecture, we show that shape-based features outperform the traditional physics-based features in the context of a multi-layer perceptron model, yielding a better 24-hour prediction accuracy.

Note that our objective in this work is not to directly compare our forecasting model with other methods, but to primarily convince the reader of the importance of shape-based features for solar flare forecasting.

Computational Geometry

To compute geometry-based features from each magnetogram, we first remove noise by filtering out pixels whose magnetic flux magnitude is below $200\ G$, then aggregate the resulting pixels into clusters if they touch along any side or corner. We then determine the number and area of each cluster, discarding all whose area is less than 10% of the maximum cluster area. We perform these operations separately for the positive ($> 200\ G$) and negative ($< -200\ G$) fields.

We then compute an *interaction factor (IF)* between all positive/negative polarity pairs, defined in a manner similar to the so-called Ising Energy used by Florios et al. (2018) (introduced first in Ahmed et al., 2010):

$$IF = \frac{B_{pos} \times B_{neg}}{r_{min}^2} \quad (1)$$

where B_{pos} and B_{neg} are the sums of the flux over the respective components and r_{min} is the smallest distance between them. A high IF value is an indication of strong, opposite-polarity regions in close proximity—an ideal configuration for a flare. Following this reasoning, we choose the pair with the highest IF value and derive a number of secondary features from it, such as the center of mass distance between the two clusters. Extraction of the most interacting pair on an example magnetogram is shown in Figure 2. Together with the values used in the computation of IF—the magnetic flux of the positive and negative clusters, the center of mass distance between them, the smallest distance between them, the interaction factor, etc.—these make up the 16-element feature vector that quantifies the interaction of the opposite polarity regions. The feature extraction process together with the final list of geometry-based features is summarized in Algorithm 1.[2]

Computational Topology

Computational topology, also known as topological data analysis (TDA) (Ghrist 2008; Kaczynski, Mischaikow, and Mrozek 2004; Zomorodian 2012), operationalizes the abstract mathematical theory of shape to allow its use with real-world data. These methods, which have been used to advantage in applications ranging from biological aggregation models (Topaz, Ziegelmeier, and Halverson 2015) to the
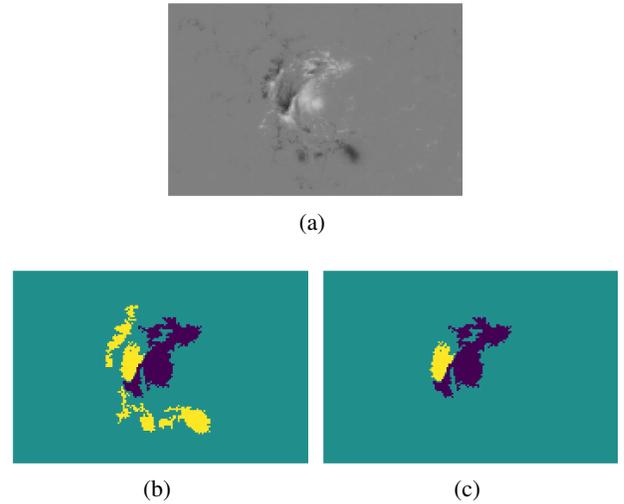
(a)

(b)   (c)

Figure 2: Process for determining the most interacting positive/negative cluster pair in geometry-based feature extraction. From a sample magnetogram shown in panel (a), positive (blue) and negative (yellow) clusters of a sufficiently large size are extracted (panel b); from these, the most interacting cluster pair is determined via calculations of the magnetic flux in each of the paired regions (panel c).

large-scale structure of the universe (Xu et al. 2019), provide a useful strategy for extracting and codifying the spatial richness of magnetograms like the ones shown in Figure 1.

The *homology* of an object formally quantifies its shape using the Betti numbers: the number of components (β_0), holes (β_1), voids (β_2), and so on. When one has a smooth, well-defined object, the textbook formulation of homology addresses this quantification, but real-world data—a finite collection of points or a set of pixels—does not really have a "shape." TDA handles this by filling in the gaps between the data points with different types of simplices. The simplest way to do this maps well to pixellated images; one can create a manifold from a selected set of pixels in an image by replacing each one by a cubical simplex—a square piece complete with its vertices and edges. This leads to the notion of connectedness amongst discrete pixels: a pair of pixels are said to be "connected" if their corresponding cubical simplices share an edge or a vertex. Such connections lead to the formation of different connected components, holes, etc.

In images where the pixel values range over some interval, it can be useful to combine this idea with thresholding. Figure 3 demonstrates the process of generating a cubical complex for a range of threshold values t.

---

[2]Please refer to Table 2 of Deshmukh et al. (2020) for a complete description.

Algorithm 1 Geometry-based Feature Extraction

1: **for** each SHARPs magnetogram image **do**
2:     Cap magnitude of all pixels to $200G$ from below, preserving the sign of each pixel.
3:     Find positive and negative flux clusters in the magnetogram.
4:     Remove clusters with area less than 10% of the maximum cluster size.
5:     **for** each pair of positive and negative clusters $\{B_{pos}, B_{neg}\}$ **do**
6:         Compute the interaction factor IF (Eqn. 1).
7:     **end for**
8:     Determine the pair with the maximum IF; call it the most interacting pair (MIP): $\{B_{pos}, B_{neg}\}^{max}$.
9:     Extract 16 geometry-based features: total positive and negative clusters in the magnetogram (2), areas of the largest positive and negative cluster (2), total magnetic fluxes of the largest positive and negative cluster (2), IF (1), MIP center of mass distance (1), MIP smallest distance (1), ratio of the MIP center of mass distance to the MIP smallest distance (1), total magnetic fluxes of the MIP clusters (2), areas of the MIP clusters (2) and total flux densities of the MIP clusters (2).
10: **end for**

Algorithm 2 Topology-based Feature Extraction

1: **for** each SHARPs magnetogram image **do**
2:     Compute β_1 persistence diagrams using a cubical complex algorithm for positive and negative flux values.
3:     Count the number of "live" β_1 holes for 20 flux values in the range $[-5000G, 5000G]$.
4: **end for**

(a) Example Image   (b) $t=0$ (c) $t=1$

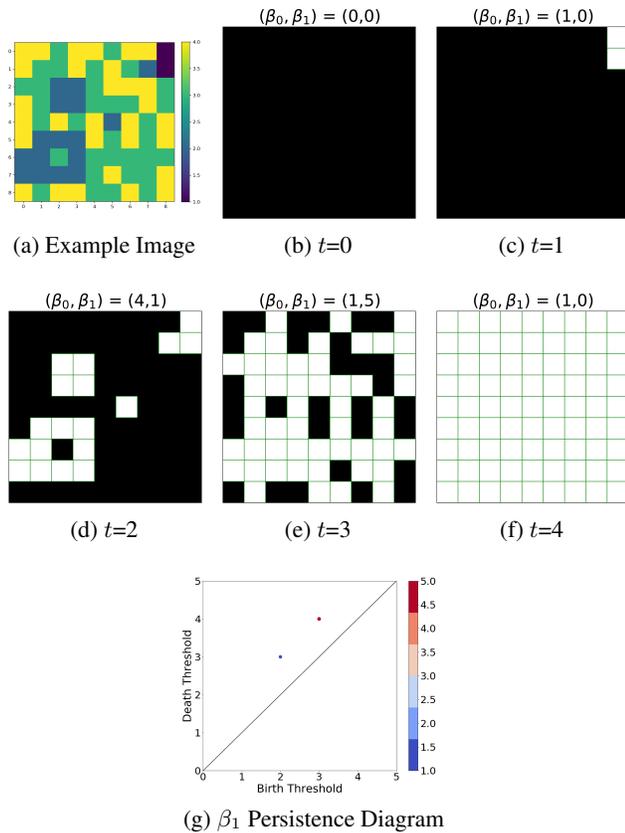(d) $t=2$ (e) $t=3$ (f) $t=4$

(g) β_1 Persistence Diagram

Figure 3: Computational topology: (a) Image-based dataset. (b)-(f) Cubical complex of that dataset for five values of sub-level thresholding ($t = [0, 1, 2, 3, 4]$). For each complex, the threshold t and the (β_0, β_1) counts are mentioned. (g): β_1 Persistence diagram.

When the threshold is low, as in Figure 3(b), none of the pixels are in the complex ($\beta_0 = 0$) and it has no holes ($\beta_1 = 0$). As t is raised and lower-value pixels enter the computation, the complex develops a small connected component at the top right ($\beta_0 = 1$). Four different components can be observed in Figure 3(d) for a threshold $t = 2$; at $t = 3$, all the components become merged together. In addition to the formation of components, two-dimensional "holes" are also formed when edges from various cubical simplices form a loop in the complex that is not filled by a cubical simplex (dark regions surrounded by green edges on all sides). We can see the presence of one and five holes, respectively, for $t = 2$ and $t = 3$.

This formation and merging of the various components and holes with changing threshold captures the shape of the set in a very nuanced way. The idea of *persistence*, first introduced in Edelsbrunner, Letscher, and Zomorodian (2000) (and independently by Robins, 2002), is that tracking that evolution allows one to deduce important information about the underlying shape that is sampled by these points. To capture all of this rich information, one can use a single plot called a *persistence diagram* (Edelsbrunner, Letscher, and Zomorodian 2000). Most components, for example, have birth and death parameter values, where they appear and disappear, respectively, from the construction. A β_0-persistence diagram has a point at (t_{birth}, t_{death}) for each component, while a β_1-persistence diagram (PD) does the same for all the holes. The β_1 PD for our toy image example is shown in Figure 3(g). Multiplicity of different holes with the same (t_{birth}, t_{death}) is represented by color; the single hole that formed at $t = 2$ and died at $t = 3$ is represented in blue, whereas the five holes corresponding to (3,4) are colored red.

The β_1 persistence diagram is the basis for our topology-based feature set. For each magnetogram, we first generate

separate PDs for the positive and negative polarities. Figure 4 shows β_1 PDs for the positive flux field in the series of magnetograms in Figure 1. The increase in the complexity of the AR between 2017-09-01 00:00:00 UT and 2017-09-05 09:00:00 UT is reflected in the patterns in the PDs: Figure 4(b) (24 hours prior to a flare) contains a far larger number of off-diagonal holes—i.e., those that persist for larger ranges of t—than Figure 4(a), which is a newly formed AR.

This visual evidence supports our claim that PDs can effectively quantify the growing complexity of a magnetogram during the lead-up to a flare. The next step is to determine whether that observation translates to discriminative power in the context of a machine-learning method. This requires one more step: vectorization of the persistence diagrams into a set of features. For this, we use a very simple method, choosing a set of 20 flux values in the interval $[-5000G, 5000G]$, and counting the number of holes that are "live" in the PDs at each of these flux values. Repeating this operation separately for the positive and negative polarities, we obtain 20 entries for our topology-based feature set. The feature extraction process is briefly summarized in Algorithm 2.

While our persistence diagram vectorization approach is relatively simple, there has been a significant effort over the last few years to more efficiently vectorize persistence diagrams for using them with ML models (Adams et al. 2017; Bubenik 2015; Carrière et al. 2019; Carrière, Cuturi, and Oudot 2017; Kusano, Fukumizu, and Hiraoka 2016). We plan to incorporate some of these techniques in future work to improve our solar flare prediction model.

Machine Learning Model

As a testbed for evaluating the different feature sets, we design a standard feedforward neural network using PYTORCH with six densely connected layers. The input layer size is variable depending on the size of the feature set; the output layer contains two neurons corresponding to the two classes—flaring and non-flaring. The four intermediate layers contain 36, 24, 16 and 8 neurons respectively, when counting from the direction of the input to the output layer. To prevent over-fitting, a Ridge Regression regularization with a penalty factor is used at each layer that limits the L_2 sum of all the weights. At each hidden layer, a *ReLU* activation is used, with a *softmax* activation applied to the final layer. We use an Adagrad optimizer for updating the model weights during the back propagation. A batch size of 128 is used in the gradient descent. The loss function used for optimization is a weighted binary cross-entropy error; since the dataset is imbalanced, a weight greater than 1 is associated with the flaring class to penalize a flare misprediction more than a non-flare misprediction. Finally, the model is trained over 15 epochs before evaluation.

Hyperparameter Tuning

For each feature set combination, we tune a number of important model hyperparameters— the learning rate, the L_2 penalty regularization factor, the cross-entropy weight ratio and the learning rate decay—to ensure that the model is optimized for the corresponding feature set and the comparison is fair. Our tuning algorithm is as follows:

1. Select 40 different hyperparameter combinations using the `python bayesopt` library (Martinez-Cantin 2014), which employs a Gaussian process-based Bayesian sampling approach.

2. Use a five-fold cross-validation approach to determine the performance of each hyperparameter combination by evaluating the average validation True Skill Statistic (TSS) metric score (Woodcock 1976) across the five folds.

3. Select the hyperparameter combination with the highest score and use it to train the model on the full training set, then evaluate this model on the test set.

This procedure is followed for all 10 training set/testing set splits of the magnetogram data described earlier. We use the `ray.tune` library (Liaw et al. 2018) to parallelize the effort of this computationally intensive task. With this setup, each tuning experiment for a single training-test combination and a single feature set takes about 5 hours on an NVIDIA Titan RTX GPU.

Results

To determine whether these geometry- and topology-based feature sets improve upon, or synergize with, the commonly used physics-based SHARPs feature sets described in the third paragraph of the introduction, we follow the procedure described in the previous section for each feature set in isolation, as well as in various combinations with the other sets.

To evaluate the results, we employ a number of standard metrics from the prediction literature: accuracy, precision, recall, True Skill Statistic (TSS), Heidke Skill Score (HSS), and frequency bias (FB). These metrics, which assess correctness in different ways, are derived from the entries of the contingency table generated by comparing the model forecast against the ground truth—True Positives (TP), False Positives (FP), False Negatives (FN) and True Negatives (TN). A description of these metrics can be found in Crown (2012) and Leka et al. (2019a). In the context of this problem, a flaring magnetogram is considered as a positive while a non-flaring magnetogram is considered a negative. For an imbalanced dataset like this, the standard accuracy metric is not very useful: a simple model that always predicted "no-flare" would have a high accuracy of 98.7%. The True Skill Statistic (TSS) score addresses this, striking an explicit balance between correctly forecasting the positive and negative samples in a highly-imbalanced dataset. TSS scores range from $[-1, 1]$, where a score of 0 indicates the model doing as well as an "always no-flare" forecast or a chance-based forecast. The Heidke Skill Score (HSS) is another normalized metric used in this literature that takes values in the range of $[-\infty, 1]$ and reports a score of 0 for a chance-based forecast. Frequency bias (FB) measures the degree of over-forecasting ($FB > 1$) or underforecasting ($FB < 1$) in the model.

The results of these evaluation experiments, which are summarized in Table 1, show that the geometry features do almost as well as, or slightly better than, the SHARPs

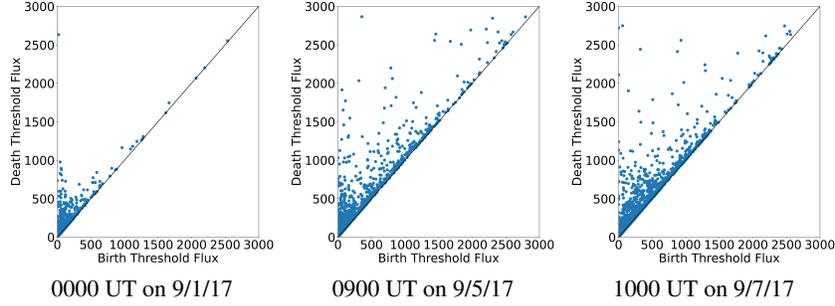| | 0000 UT on 9/1/17 | 0900 UT on 9/5/17 | 1000 UT on 9/7/17 |

Figure 4: β_1 persistence diagrams for the magnetograms of Figure 1, constructed from the set of pixels with positive magnetic flux densities using the cubical complex approach. These diagrams reveal a clear change in the topology of the field structure well before the major flare that was generated by this active region at 0910 UT on 6 September 2017.

	Accuracy	Precision	Recall	FB	TSS	HSS
Perfect score	1	1	1	1	1	1
SHARPs (19)	0.84 ± 0.02	0.06 ± 0.01	0.87 ± 0.05	13.84 ± 1.93	0.70 ± 0.01	0.09 ± 0.02
Geometry (16)	0.82 ± 0.01	0.06 ± 0.01	0.89 ± 0.04	14.89 ± 1.15	0.71 ± 0.04	0.09 ± 0.01
Topology (20)	0.86 ± 0.02	0.08 ± 0.01	$\mathbf{0.90 \pm 0.02}$	12.20 ± 1.96	$\mathbf{0.75 \pm 0.03}$	0.12 ± 0.02
SHARPs + Geometry (35)	0.84 ± 0.02	0.07 ± 0.01	0.89 ± 0.05	13.24 ± 1.98	0.73 ± 0.03	0.11 ± 0.01
SHARPs + Topology (39)	$\mathbf{0.86 \pm 0.01}$	$\mathbf{0.08 \pm 0.01}$	0.89 ± 0.03	$\mathbf{11.55 \pm 1.06}$	$\mathbf{0.75 \pm 0.03}$	$\mathbf{0.12 \pm 0.01}$
All three sets (55)	$\mathbf{0.86 \pm 0.01}$	$\mathbf{0.08 \pm 0.01}$	0.87 ± 0.04	11.77 ± 1.27	0.74 ± 0.03	0.11 ± 0.01

Table 1: Performance of the various feature sets. Numbers in paranthesis indicate the number of elements in the input feature vector. For all the metrics except for frequency bias (FB), higher is better.

features, whereas the topology features outperform the SHARPs features by a significant margin, as assessed by the TSS score (≈ 0.05). Combining the shape-based features with the physics-based features reveals some useful synergies: all of the pairwise-combined feature sets outperform the individual feature sets. The size of the improvement varies: the effect is somewhat stronger when geometry-based features are involved. Interestingly, combining all three feature sets does slightly worse than the SHARPs-topology combination: that is, simply using more features does not guarantee better performance, a trend that has been noted in the flare-forecasting literature, e.g. Jonas et al. (2018). These improvement trends are visible across all of the metrics in the table.

To summarize: *the shape-based features outperform and/or supplement the predictive power of the SHARPs features.* In the context of our MLP model, this is a particularly striking result: abstract shape-based features automatically extracted from the magnetic field of an active region do as well or even better than handcrafted features viewed by experts as relevant to the physics of an active region and the flaring process.

A look at the other metrics in Table 1 shows that tuning the model for the TSS can impact some of the other metrics. A value of $FB > 1$—i.e., low scores for precision and high scores for recall—indicates a high percentage of false positives (FP) and a low percentage of false negatives (FN). That is, our model is essentially an overforecasting model: it sacrifices false alarms (FP) in order to lower missed events (FN). This is a trend observed in other flare-prediction models in the literature, such as DeepFlareNet (Nishizuka et al. 2018). Via further investigation, we found that this is the consequence of tuning the binary cross-entropy loss function weight. As a consequence of tuning for the TSS metric, this parameter takes on high values (> 150), causing the model to err on the side of correctly forecasting the flaring magnetograms. With our hyperparameter tuning framework, it is possible to optimize for some other metric based on the priorities of the forecaster.

Deployment

Deployment is a major aim for us, since this research is proceeding in the Space Weather Technology Research and Education Center, an organization that has a strong focus on transitioning research models and tools to operations. Both NOAA's Space Weather Prediction Center (a division of the

National Weather Service) and NASA's Community Coordinated Modeling Center have capabilities for comparative validation of various space weather forecasting tools. We will submit our final model for comparison against other solar flare forecasting systems to one or both of these government organizations for comparative validation. As in terrestrial weather forecasting, it is ultimately up to the National Weather Service which tools they choose to deploy, and those judgments are based not only on quantitative metric comparisons but on ease of use in their human-in-the-loop operational forecasting environment. We are also in discussions with the UK Met Office for evaluation and deployment of several forecasting innovations including this solar flare prediction model.

As an initial step for deployment, we compared our model with the operational flare-forecasting models evaluated in Leka et al. (2019a). We used a dataset similar to the one used in that paper (training set: 2010-2015, testing set: 2016-2017), trained our shape-based model using topological and SHARPs feature sets, and limited our comparison to the M1.0+/24hr flare forecasting problem (see the top panel of Figure 5, Leka et al., 2019a). When tuned on the TSS metric, our proposed shape-based model returns a TSS score of 0.78, outperforming all the existing operational systems (TSS = [0-0.5]). However, our model produces a high FB score of 20.62 (i.e., overforecasting), and performs poorly on other metrics such as accuracy (0.89). In comparison, the existing forecasting systems report an FB score in the range of [0-1.5] and an accuracy of approximately 0.95 (excluding a single outlier). Optimizing our shape-based model on the precision metric, on the other hand, reduces the false positives to 0, improving the accuracy (0.995) and FB (0.30) and making them on par with or better than the operational forecasting models. This comes at the cost of a lowered TSS score (0.30).

Conclusions

In this work, we introduced novel shape-based features constructed using tools from computational geometry and computational topology. We successfully demonstrated their higher forecasting capability when compared to the physics-based features that are traditionally used in the context of a multi-layer perceptron model. This is an important result for ML-based solar flare forecasting research, and a stronger result than many other feature comparison approaches—for example Chen et al. (2019), which showed that CNN autoencoder-extracted features from magnetograms did as well as SHARPs-based features.

Our future directions will focus on alternative modeling approaches, improved feature engineering, and metric optimization strategies. More specifically, this will include validating our results with alternative ML models (LSTMs, SVMs), improved featurization/vectorization of persistence diagrams, performing multivariate feature ranking to understand feature relevance with solar flares and finally, investigating optimization trade-offs over the different metrics using our hyperparameter tuning framework. The feature engineering methodology in this work will eventually be integrated into a hybrid solar flare forecasting model that will use CNN-extracted features from solar magnetic and atmopsheric data in combination with the physics- and shape-based features.

References

Adams, H.; et al. 2017. Persistence Images: A Stable Vector Representation of Persistent Homology. *J. Mach. Learn. Res.* 18(1): 218–252. ISSN 1532-4435. doi:10.5555/3122009.3122017.

Ahmed, O. W.; et al. 2010. A new technique for the calculation and 3D visualisation of magnetic complexities on solar satellite images. *The Visual Computer* 26(5): 385–395. doi:10.1007/s00371-010-0418-1.

Barnes, G.; et al. 2016. A comparison of flare forecasting methods. I. Results from the "All-Clear "Workshop. *The Astrophysical Journal* 829(2): 89. doi:10.3847/0004-637x/829/2/89.

Benvenuto, F.; et al. 2018. A Hybrid Supervised/Unsupervised Machine Learning Approach to Solar Flare Prediction. *Astrophysical Journal* 853(1): 90. doi:10.3847/1538-4357/aaa23c.

Bobra, M. G.; and Couvidat, S. 2015. Solar Flare Prediction Using SDO/HMI Vector Magnetic Field Data with a Machine-Learning Algorithm. *The Astrophysical Journal* 798(2): 135. doi:10.1088/0004-637x/798/2/135.

Bobra, M. G.; et al. 2014. The Helioseismic and Magnetic Imager (HMI) Vector Magnetic Field Pipeline: SHARPs – Space-Weather HMI Active Region Patches. *Solar Physics* 289(9): 3549–3578. doi:10.1007/s11207-014-0529-3.

Boucheron, L. E.; Al-Ghraibah, A.; and McAteer, R. T. J. 2015. Prediction of Solar Flare Size and Time-to-Flare Using Support Vector Machine Regression. *Astrophysical Journal* 812: 51. doi:10.1088/0004-637X/812/1/51.

Bubenik, P. 2015. Statistical Topological Data Analysis Using Persistence Landscapes. *J. Mach. Learn. Res.* 16(1): 77–102. ISSN 1532-4435. doi:10.5555/2789272.2789275.

Campi, C.; et al. 2019. Feature Ranking of Active Region Source Properties in Solar Flare Forecasting and the Uncompromised Stochasticity of Flare Occurrence. *Astrophysical Journal* 883(2): 150. doi:10.3847/1538-4357/ab3c26.

Carrière, M.; Cuturi, M.; and Oudot, S. 2017. Sliced Wasserstein Kernel for Persistence Diagrams. *arXiv e-prints* arXiv:1706.03358.

Carrière, M.; et al. 2019. PersLay: A Simple and Versatile Neural Network Layer for Persistence Diagrams. *arXiv e-prints* arXiv:1904.09378.

Chen, Y.; et al. 2019. Identifying Solar Flare Precursors Using Time Series of SDO/HMI Images and SHARP Parameters. *Space Weather* 17(10): 1404–1426. ISSN 1542-7390. doi:10.1029/2019SW002214.

Crown, M. D. 2012. Validation of the NOAA Space Weather Prediction Center's Solar Flare Forecasting Look-up Table and Forecaster-Issued Probabilities. *Space Weather* 10(6). doi:10.1029/2011SW000760.

Deshmukh, V.; et al. 2020. Leveraging the mathematics of shape for solar magnetic eruption prediction. *Journal of Space Weather and Space Climate* 10: 13. doi:10.1051/swsc/2020014.

Edelsbrunner, H.; Letscher, D.; and Zomorodian, A. 2000. Topological Persistence and Simplification. *Discrete & Computational Geometry* 28: 511–533. doi:10.1007/s00454-002-2885-2.

Florios, K.; et al. 2018. Forecasting Solar Flares Using Magnetogram-based Predictors and Machine Learning. *Solar Physics* 293(2): 28. doi:10.1007/s11207-018-1250-4.

Ghrist, R. 2008. Barcodes: The Persistent Topology of Data. *Bulletin of the American Mathematical Society* 45(1): 61–75. doi:10.1090/S0273-0979-07-01191-3.

Hale, G. E.; et al. 1919. The Magnetic Polarity of Sun-Spots. *The Astrophysical Journal* 49: 153. doi:10.1086/142452.

Huang, X.; et al. 2018. Deep Learning Based Solar Flare Forecasting Model. I. Results for Line-of-sight Magnetograms. *Astrophysical Journal* 856(1): 7. doi:10.3847/1538-4357/aaae00.

Jonas, E.; et al. 2018. Flare Prediction Using Photospheric and Coronal Image Data. *Solar Physics* 293(3): 48. doi:10.1007/s11207-018-1258-9.

Kaczynski, T.; Mischaikow, K.; and Mrozek, M. 2004. *Computational Homology*, volume 157 of *Applied Mathematical Sciences*. New York: Springer-Verlag. doi:10.1007/b97315.

Kusano, G.; Fukumizu, K.; and Hiraoka, Y. 2016. Persistence Weighted Gaussian Kernel for Topological Data Analysis. *arXiv e-prints* arXiv:1601.01741.

Leka, K. D.; et al. 2019a. A Comparison of Flare Forecasting Methods. II. Benchmarks, Metrics, and Performance Results for Operational Solar Flare Forecasting Systems. *Astrophysical Journal* 243(2): 36. doi:10.3847/1538-4365/ab2e12.

Leka, K. D.; et al. 2019b. A Comparison of Flare Forecasting Methods. III. Systematic Behaviors of Operational Solar Flare Forecasting Systems. *Astrophysical Journal* 881(2): 101. doi:10.3847/1538-4357/ab2e11.

Liaw, R.; et al. 2018. Tune: A Research Platform for Distributed Model Selection and Training. *arXiv e-prints* arXiv:1807.05118.

Martinez-Cantin, R. 2014. BayesOpt: A Bayesian Optimization Library for Nonlinear Optimization, Experimental Design and Bandits. *J. Mach. Learn. Res.* 15(1): 3735–3739. ISSN 1532-4435. doi:10.5555/2627435.2750364.

Maynard, T.; Smith, N.; and Gonzalez, S. 2013. Solar storm risk to the North American electric grid. Technical report, Lloyd's.

McIntosh, P. S. 1990. The Classification of Sunspot Groups. *Solar Physics* 125: 251–267. doi:10.1007/BF00158405.

Nishizuka, N.; et al. 2017. Solar Flare Prediction Model with Three Machine-Learning Algorithms using Ultraviolet Brightening and Vector Magnetograms. *Astrophysical Journal* 835: 156. doi:10.3847/1538-4357/835/2/156.

Nishizuka, N.; et al. 2018. Deep Flare Net (DeFN) Model for Solar Flare Prediction. *Astrophysical Journal* 858(2): 113. doi:10.3847/1538-4357/aab9a7.

Park, E.; et al. 2018. Application of the Deep Convolutional Neural Network to the Forecast of Solar Flare Occurrence Using Full-disk Solar Magnetograms. *Astrophysical Journal* 869(2): 91. doi:10.3847/1538-4357/aaed40.

Robins, V. 2002. Computational Topology for Point Data: Betti Numbers of α-Shapes. In Mecke, K.; and Stoyan, D., eds., *Morphology of Condensed Matter*, volume 600 of *Lecture Notes in Physics*, 261–274. Springer Berlin Heidelberg. doi:10.1007/3-540-45782-8_11.

Schrijver, C. J. 2016. The Nonpotentiality of Coronae of Solar Active Regions, the Dynamics of the Surface Magnetic Field, and the Potential for Large Flares. *Astrophysical Journal* 820(2): 1–17. doi:10.3847/0004-637x/820/2/103.

Topaz, C. M.; Ziegelmeier, L.; and Halverson, T. 2015. Topological Data Analysis of Biological Aggregation Models. *PLOS ONE* 10(5): 1–26. doi:10.1371/journal.pone.0126383.

Woodcock, F. 1976. The Evaluation of Yes/No Forecasts for Scientific and Administrative Purposes. *Monthly Weather Review* 104(10): 1209–1214. doi:10.1175/1520-0493(1976)104⟨1209:TEOYFF⟩2.0.CO;2.

Xu, X.; et al. 2019. Finding Cosmic Voids and Filament Loops Using Topological Data Analysis. *Astron. Comput.* 27: 34–52. doi:10.1016/j.ascom.2019.02.003.

Yang, X.; et al. 2013. Magnetic Nonpotentiality in Photospheric Active Regions as a Predictor of Solar Flares. *The Astrophysical Journal* 774(2): L27. doi:10.1088/2041-8205/774/2/l27.

Yu, D.; et al. 2010. Short-Term Solar Flare Level Prediction Using a Bayesian Network Approach. *The Astrophysical Journal* 710(1): 869. doi:10.1088/0004-637x/710/1/869.

Yuan, Y.; et al. 2010. Solar Flare Forecasting using Sunspot-Groups Classification and Photospheric Magnetic Parameters. *Proceedings of the International Astronomical Union* 6: 446 – 450. doi:10.1017/S1743921311015742.

Zheng, Y.; Li, X.; and Wang, X. 2019. Solar Flare Prediction with the Hybrid Deep Convolutional Neural Network. *Astrophysical Journal* 885(1): 73. doi:10.3847/1538-4357/ab46bd.

Zomorodian, A. 2012. *Topological Data Analysis*, volume 70 of *Advances in Applied and Computational Topology*. Providence: American Mathematical Society. doi:10.5555/2408007.